Journal of Nuclear Materials 401 (2010) 1–12

Contents lists available at ScienceDirect

Journal of Nuclear Materials

journal homepage: www.elsevier.com/locate/jnucmat

Isotope dependence of chemical erosion of carbon

C.O. Reinhold [a,b,*], P.S. Krstic [a,b], S.J. Stuart [c], H. Zhang [a], P.R. Harris [a], F.W. Meyer [a]

[a] Physics Division, Oak Ridge National Laboratory, Oak Ridge, TN 37831-6372, USA
[b] Department of Physics, University of Tennessee, Knoxville, TN 37996, USA
[c] Department of Chemistry, Clemson University, Clemson, SC 29634, USA

ARTICLE INFO

Article history:
Received 20 November 2009
Accepted 16 March 2010

ABSTRACT

We study the chemical erosion of hydrogen-supersaturated carbon due to bombardment by hydrogen isotopes H, D, and T at energies of 1–30 eV using classical molecular dynamics simulations. The chemical structure at the hydrogen-saturated interface (the distribution of terminal hydrocarbon moieties, in particular) shows a weak dependence on the mass of the impinging atoms. However, the sputtering yields increase considerably with increasing projectile mass. We analyze the threshold energies of chemical sputtering reaction channels and show that they are nearly mass independent, as expected from elementary bond-breaking chemical reactions involving hydrocarbons. Chemical sputtering yields for D impact are compared with new experimental data. Good agreement is found for small hydrocarbons but the simulations overestimate the production of large hydrocarbons for energies larger than 15 eV. We present a thorough analysis of the dependence of our simulations on the parameters of the bombardment schemes and discuss open questions and possible avenues for development.

1. Introduction

Understanding the interactions of plasma particles with plasma-facing materials is of crucial importance for the development of future fusion devices such as ITER and DEMO. These interactions lead to surface erosion, particle deposition and plasma pollution, degrading fusion performance and leading to long-term tritium retention. Carbon-based divertor tiles are common in many existing fusion machines as well as in the current phase of ITER. Plasma-surface processes which involve interactions of hydrogen isotopes with carbon may play an important role in these machines [1–4].

Chemical sputtering is the dominant carbon erosion mechanism in collisions of low-energy (below ~50 eV) H, D, and T with carbon. Cumulative bombardment by hydrogen isotopes breaks and passivates bonds and leads to the formation of stable hydrocarbon terminal moieties that can be collisionally detached or desorbed thermally. Swift chemical sputtering is a process where particles are ejected as a result of a chemical reaction that takes place near the end of the path traveled by the impinging projectile. Identifying the dominant reactions leading to emission of specific hydrocarbons has been the goal of numerous papers dating back over four decades (e.g. [5–7]). At high impact energies a complex collision cascade takes place and carbon erosion can be described in terms of "physical sputtering", i.e. a sequence of binary atom–atom collisions as in the TRIM.SP code [8]. However, for impact energies near the thresholds for breaking the C–C bonds that attach the moieties, most of the projectile energy is used in the end-point chemical reaction that breaks these bonds and chemical sputtering is the dominant ejection process.

Low-energy experiments in the regime where chemical sputtering dominates are challenging to perform for atomic hydrogen (deuterium) ions, due to falling beam intensities with decreasing energy, and only a few measurements exist [11–13]. Most reported low-energy chemical sputtering yields have been obtained using molecular $H_2^+(D_2^+)$ or $H_3^+(D_3^+)$ beams, but reported as H^+ or D^+ impact data at one half or one third the impact energy of the diatomic or triatomic ion, with the corresponding yields normalized to the number of constituent atoms of the molecule [11–15]. In an attempt to bridge existing gaps and extend the data to yet lower energies, molecular dynamics (MD) simulations have tackled this problem in recent years, using the available experimental data above 10 eV for validation. Early simulations were partially successful in describing the total carbon erosion yield using hydrogenated surfaces with a uniform distribution of hydrogen and carbon having an H/C ratio of ~0.4 [9,10], corresponding to the experimentally determined equilibrium H saturation density in bulk graphite [16]. However, these simulations predicted a spectrum of ejected hydrocarbons that was not consistent with experimental observations for surfaces hydrogenated by cumulative bombardment, which enhances considerably the hydrogen content of the near-surface region [9,10,17]. More recent simulations have shown that the individual yields of ejecta change dramatically as the

* Corresponding author at: Physics Division, Oak Ridge National Laboratory, Oak Ridge, TN 37831-6372, USA. Tel.: +1 865 574 4579; fax: +1 865 574 1118.
E-mail address: reinhold@ornl.gov (C.O. Reinhold).

0022-3115/$ - see front matter © 2010 Elsevier B.V. All rights reserved.
doi:10.1016/j.jnucmat.2010.03.012

surfaces are supersaturated by cumulative bombardment [18–22], which results in the ejection of larger and more saturated molecules and yields a better agreement with experimental findings for the simplest hydrocarbons. The chemical composition of these supersaturated surfaces was shown to depend not only on the fluence but also on the impact energy, kind of species and even on the internal state of the incident projectiles.

In this work we further analyze the dependence of simulated sputtering on the different parameters associated with our cumulative bombardment scheme and investigate how the different masses of the hydrogen isotopes influence the sputtering yields and surface chemistry. With the exception of the near-threshold region, isotope effects for carbon erosion are expected, since heavier projectiles can transfer a larger fraction of their energy to individual carbon atoms in binary collisions. For example, a projectile with mass M_P that undergoes a head-on binary collision with a carbon atom with mass M_C ($>M_P$) delivers a maximum energy transfer

$$\Delta E_C = \frac{4M_P M_C}{(M_P + M_C)^2} E_P, \quad (1)$$

where E_P is the incident projectile energy. For D (T) projectiles ΔE_C is a factor of 1.72 (2.25) larger than that for H projectiles, which influences the probability for breaking C–C bonds at a given E_P [2]. Estimates for $E_P > 50$ eV predict that the sputtering yield for D impact should be a factor of ~3 larger than that for H impact [2,3,23]. At lower impact energies, where chemical sputtering dominates, some models have predicted similar moderate enhancements [2,9] while others foresee a much bigger enhancement [3]. One set of molecular dynamics simulations has surprisingly seen very little isotopic enhancement of sputtering yield [24,25], although this may be due to the lack of thermalization and high effective temperature in these simulations, leading to thermal rather than collisional effects [25]. Our calculations are consistent with a moderate enhancement and we show that similar (moderate) isotope effects are found in the most basic bond-breaking collisions of H, D, and T with hydrocarbons. These simpler collision systems afford the opportunity to study isotope effects near the thresholds for breaking C–C bonds, where the statistics in typical MD simulations are very poor. We show that the dominant channel at the lowest threshold for breaking C–C bonds is always an associative–dissociative reaction where the projectile attaches to one of the ejected C atoms. Furthermore, we show that the threshold energy for all C–C bond-breaking reaction channels is mass independent and cannot be described in terms of energy and momentum transfers in binary projectile-target-atom collisions (e.g. Eq. (1)).

The calculated isotope dependences at room temperature are compared with the available data [4,12,14,15]. In addition, the calculated sputtering yields for D impact and for families of ejected hydrocarbon molecules containing one, two, or three carbon atoms are compared with new experimental data. We show that there are a number of open questions and disagreements between theory and experiment and discuss possible avenues for future development.

2. Molecular dynamics simulations

Details of our simulations can be found elsewhere [18–21]. Thus, only a brief description is presented here. All molecular dynamics (MD) simulations in this paper refer to normal incidence of the hydrogen projectiles on a surface at a temperature of 300 K and were performed with the most recent version of the reactive empirical bond-order (REBO) potential [27]. The surface normal is along the +z axis and impact particles were introduced at a large distance from the surface at a random position uniformly distributed in the surface plane (the x–y plane) and with a given kinetic energy.

We perform two types of molecular dynamics (MD) simulations. The first one is devoted to preparing supersaturated surfaces by cumulative bombardment while a second series of simulations is used to calculate the sputtering yields for these prepared surfaces from a large number of single, independent projectile impacts. Particles in the bottom 2 Å of the simulation cell in both types of simulations were held rigid in the z direction in order to avoid net center of mass motion with repeated impacts while a Langevin thermostat is applied along the x and y directions.

In each case, we follow the interactions of H, D, and T projectiles impinging on hydrogenated surfaces that have been supersaturated self-consistently using the same isotope mass and energy of the projectile, i.e., H on a-C:H, D on a-C:D, and T on a-C:T (where a-C:H is short for hydrogenated amorphous carbon). We also perform calculations using H_2^* and D_2^* vibrationally excited molecules impinging on surfaces that have been supersaturated self-consistently by H_2^* and D_2^* bombardment.

2.1. Cumulative bombardment simulations and surface evolution

The simulations start from an initial cell that approximates the bulk properties of amorphous hydrogenated carbon [18]. Our initial cell has a density of 2.0 g cm^{-3}, a H/C ratio of 0.4 (700 H, D, or T atoms and 1750 C atoms), a side length of 26.5 Å and periodic boundary conditions in all directions. The periodic boundary conditions were then removed in the z direction, generating a 2-dimensional periodic slab, and the surface was relaxed for 100 ps to remove any instabilities. The resulting surface was the starting point for the subsequent preparation of supersaturated carbon surfaces by H, D, T, H_2^* and D_2^* bombardment. Using a pre-hydrogenated surface as a starting point dramatically reduces the fluence needed to reach a supersaturation regime resembling experiments [18–21]. Fig. 1 illustrates the evolution of the simulation cell as a function of scaled D "fluence", the latter being equivalent to the number of cumulative projectile impacts, N_p^{cum}. (The actual fluence=N_p^{cum}/surface area for 1000 D impacts is equal to 1.4×10^{20} D m^{-2}.)

Prior to any impact (Fig. 1a) the cell consists of a nearly uniform, densely packed distribution of D and C atoms. For increasing fluence surface swelling takes place and long filamentous structures extending above the initial surface develop (Fig. 1b). At the same time, the position of the "interface" (indicated by blue lines) changes. We define the position of the interface, $z_{int}(N_p^{cum})$, as the z coordinate where the density of carbon atoms is one half of the bulk density. It is noteworthy that for impact energies above ~15 eV long filamentous structures of atoms are formed that extend for tens of Angstroms above this interface (e.g. Fig. 1c). After ~1000 impacts the densities of C atoms (Fig. 1d) and D atoms (Fig. 1e) enter a quasi steady-state regime where $z_{int}(N_p^{cum})$ linearly decreases with N_p^{cum} purely as a consequence of surface erosion. After ~1000 impacts the region around the interface becomes a D-rich layer that remains nearly constant in width and evolves downward as the surface is eroded (Fig. 1e). In this interface region the D/C ratio is close to unity and the D-saturated carbon atoms provide the precursors for emission of saturated hydrocarbons. For the present range of impact energies the majority of projectiles are implanted within ~10 Å of the interface.

Fig. 1d shows that the amount of unmodified bulk material within the simulation cell vanishes after a few thousand impacts. This imposes an upper limit on the impact energies that can be studied for a given cell size. In this work we focus on the sputtering yields for surfaces created by cumulative bombardment in the range $1000 < N_p^{cum} < 2000$ where a quasi steady-state (supersaturated) regime is approximately reached for all projectiles. Fig. 2

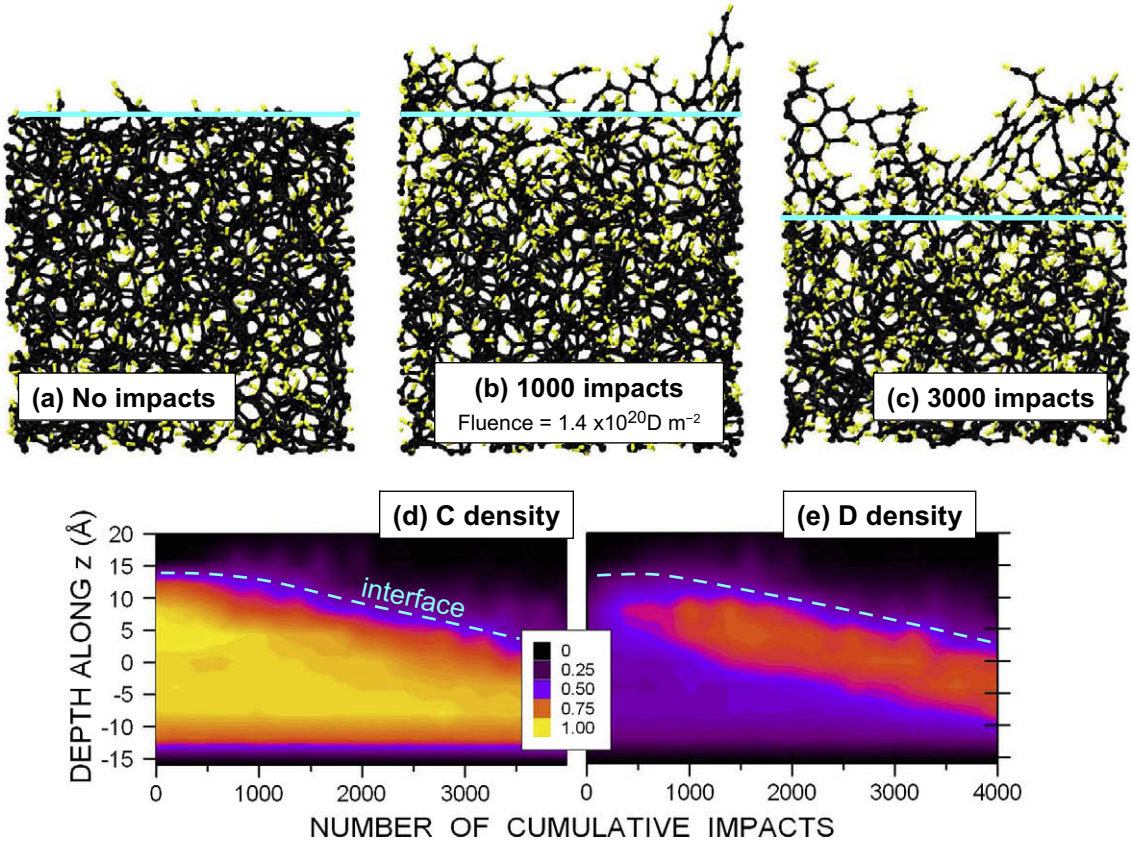

Fig. 1. (a–c) Evolution of the simulation cell during cumulative bombardment by D atoms with an impact energy of 20 eV. The yellow (black) spheres denote deuterium (carbon) atoms. The horizontal lines denote the position of the interface, ($z_{int} N_p^{cum}$) (see text). (d and e) Development of the densities of carbon atoms, $\rho_C(z, N_p^{cum})$, and deuterium atoms, $\rho_D(z, N_p^{cum})$, in the simulation cell as a function of the number of cumulative D impacts, N_p^{cum}. The light blue dashed lines denote the position of the interface (see text). A depth $z = 0$ represents the midpoint of the initial cell. Both the carbon and deuterium densities are expressed as a fraction of the bulk carbon densities prior to bombardment: i.e. the color coding shows the ratios $\rho_C(z, N_p^{cum})/\rho_C(0,0)$ and $\rho_D(z, N_p^{cum})/\rho_C(0,0)$ (see scale in the inset). (For interpretation of the references to colour in this figure legend, the reader is referred to the web version of this article.)

shows that this range is questionable at 30 eV. For 30 eV H impact the surfaces have not completely entered a steady state of erosion at $N_p^{cum} \sim 1000$ while the simulation cell is excessively eroded by cumulative 30 eV T impact at $N_p^{cum} \sim 2000$. Already evident from the figures is that T impact leads to a considerable larger rate of erosion than H impact, i.e. a clear isotope effect.

Reaching such supersaturated surfaces required total cumulative bombardment times of several ns. This time is sufficient to reach a quasi-steady state comparable to that achieved after tens of minutes in the experiment. Consequently, the simulated flux ($\sim 10^{29}$ D m^{-2} s^{-1}) is much larger, by many orders of magnitude, than that typical beam experiments or even fusion applications (see [18,21] for a more detailed discussion). Sample heating at such large fluxes was avoided by properly dissipating the energy deposited after each impact. This was accomplished by allowing particles to evolve freely during a finite time interval Δt_F immediately after introduction of a projectile and subsequently applying a Langevin thermostat for a time interval Δt_T to the entire cell until it reaches the background temperature of 300 K [18,21]. (A time constant of 100 fs for the thermostat was sufficient to remove the excess thermal energy that resulted from the impact within $\Delta t_T = 1$ ps.) The choice of Δt_F was determined by requiring that the vast majority of sputtered particles were able to "escape" the surface during this time. We use the terminology "escape" to indicate atoms and molecules that become detached from the main simulation cell, are above the interface ($z > z_{int}$), and have positive normal velocities $v_z > 0$. Because the REBO potential has cutoff radii $R_c = 2.0$ Å for all C–C interactions, a molecule is considered to be detached from the cell when the smallest distance between atoms in the molecule and atoms in the cell is larger than R_c. It is noteworthy that, since long filamentous structures are formed above the interface, some detached molecules need a much longer time to reach z coordinates exceeding those of all atoms in the cell.

Our choice for Δt_F was finalized after verifying that the prepared surface characteristics were not too sensitive to changes of this parameter. Fig. 3 shows that the value $\Delta t_F = 2$ ps is a reasonable choice since the surface characteristics are relatively stable around this value, which is consistent with the time scales for prompt emission found by other authors [9,10]. The figure also illustrates our analysis of the changing surface characteristics during cumulative bombardment that play a key role in chemical sputtering. The left side frames (a) and (b) display the total number of C and D atoms, respectively, and show that the former decreases monotonically while considerable numbers of D atoms are initially retained in the surface. Retention occurs as D atoms break and passivate bonds, leading to the formation of saturated moieties near the interface. The right-side frames of Figs. 3c and 3d show that the number of R–CD_2 and R–CD_3 terminal moieties near the interface increase with the number of impacts and start saturating at around 1000 impacts. These numbers are calculated from the coordination number of each atom defining its neighbors as those that are at located at a distance smaller than the REBO cutoff radii. The interface region where the number of moieties are analyzed corresponds to atoms with $z > z_{int} - 10$ Å. A complementary analysis of

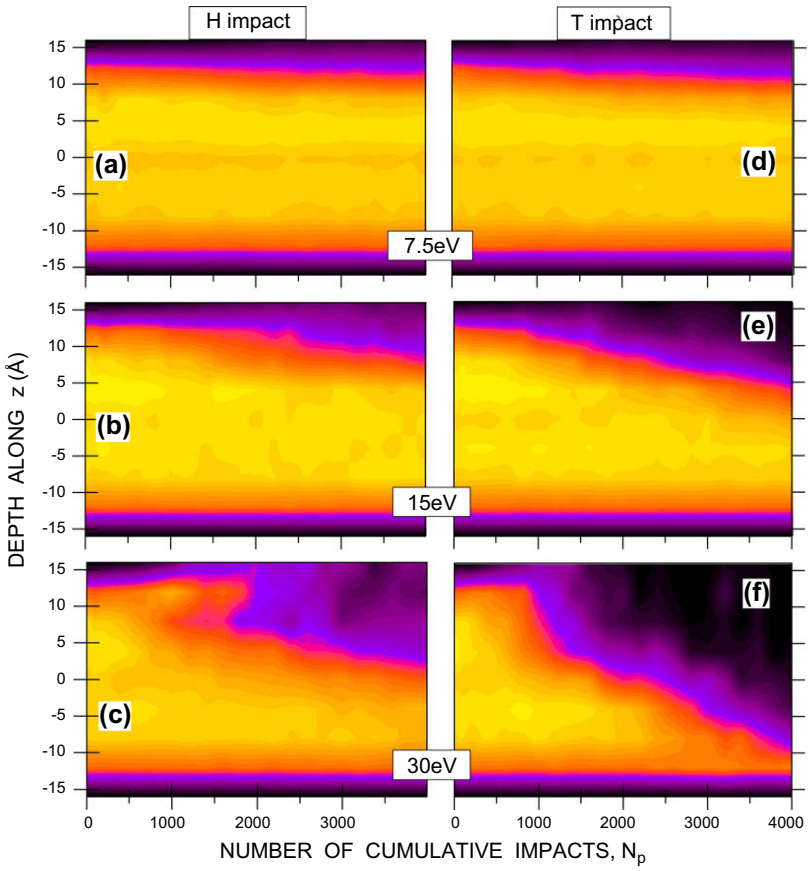

Fig. 2. Development of the density of carbon atoms in the simulation cell as a function of the number of cumulative H or T impacts at various energies. The color coding is the same as in Fig. 1. (For interpretation of the references to colour in this figure legend, the reader is referred to the web version of this article.)

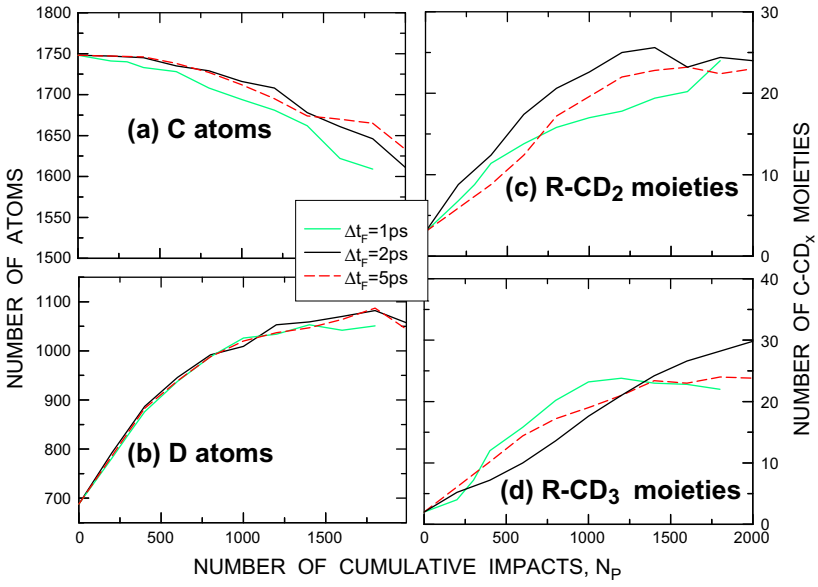

Fig. 3. Number of (a) C atoms and (b) D atoms in the simulation cell and (c) R–CD_2 and (d) R–CD_3 terminal moieties in the interface region ($z > z_{int} - 10$ Å) as a function of the number of cumulative impacts of D atoms with an impact energy of 15 eV. The various curves correspond to three different bombardment schemes with Δt_F = 1, 2, 5 ps (see text). The differences between the curves for different Δt_F values are not statistically significant (i.e. these differences are comparable to the differences between different random sequences of cumulative impacts).

the R–CD_x terminal moieties for different surface regions and a discussion of the correlation between the number of moieties and the erosion yields can be found in [18].

Figs. 4 and 5 show the dependence of the surface characteristics on the mass of the projectile. The rate of erosion, inferred from the decreasing number of C atoms in the cell, clearly increases with the

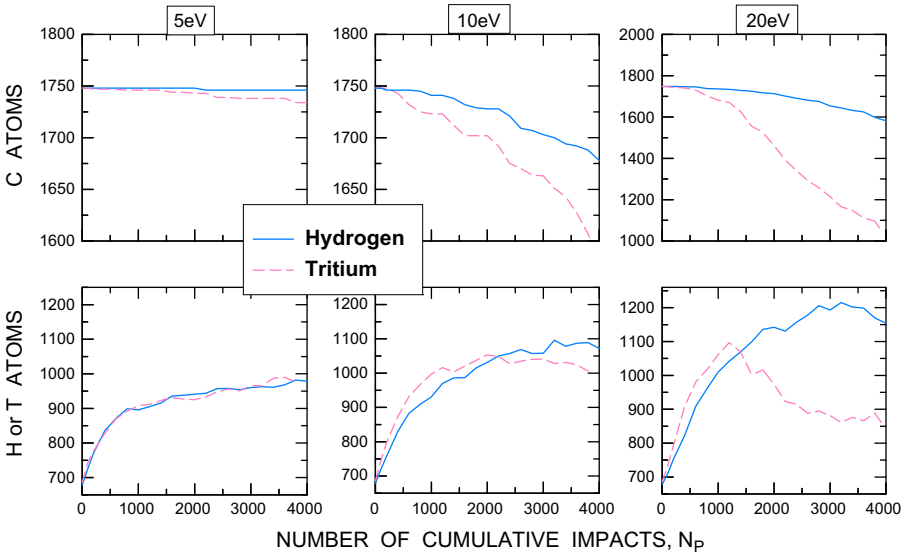

Fig. 4. Number of C and H or T atoms in the simulation cell as a function of the number of cumulative H or T impacts for three impact energies.

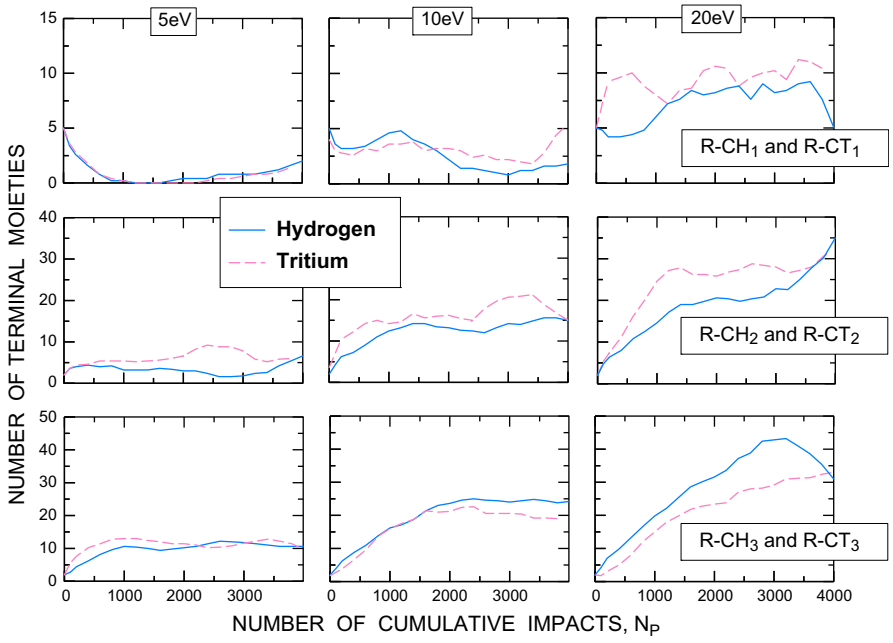

Fig. 5. Number of terminal moieties in the interface region ($z > z_{int} - 10$ Å) as a function of the number of cumulative H or T impacts for three impact energies. The differences between the curves for H and T are not statistically significant (i.e. these differences are comparable to the differences between different random sequences of cumulative impacts).

mass of the projectile (see Fig. 4). Because the emission of hydrocarbons proceeds in two steps, namely the production of terminal moieties followed by the breaking of C–C bonds, it is important to identify the relative role of each step. Fig. 5 shows that the distribution of moieties near the interface is not dramatically different. This implies that the increased erosion for increasing mass is not due to an increased production of terminal moieties but rather to a larger probability of breaking the C–C bonds that attach the molecules to the surface. A more extensive discussion about isotope effects is presented in Section 3.

2.2. Particle emission yields

Particle emission yields are calculated here employing two different approaches: (a) using the cumulative impact simulations and (b) using non-cumulative independent particle impacts on surfaces prepared by cumulative impact. Large yields can be obtained from the former but the latter is needed to compute small yields (see below).

Within the cumulative simulation, the yield for emitting a given ejecta, Y_{ejec}, at an average fluence $N_p^{av} = \langle N_p^{cum} \rangle$ is calculated from the total number of ejecta, N_{ejec}, resulting from 1000 consecutive impacts in the interval $-500 < N_p^{cum} - N_p^{av} < 500$ impacts (i.e. $Y_{ejec} = N_{ejec}/1000$). A standard error can be estimated by splitting this interval in five intervals of 200 impacts and calculating the standard deviation of the yields obtained in each interval. This approach is sufficient to compute statistically significant particle emission yields for large quantities such as reflection coefficients or total carbon erosion yields. (by significant we mean that the yields are considerably bigger than their standard error). However,

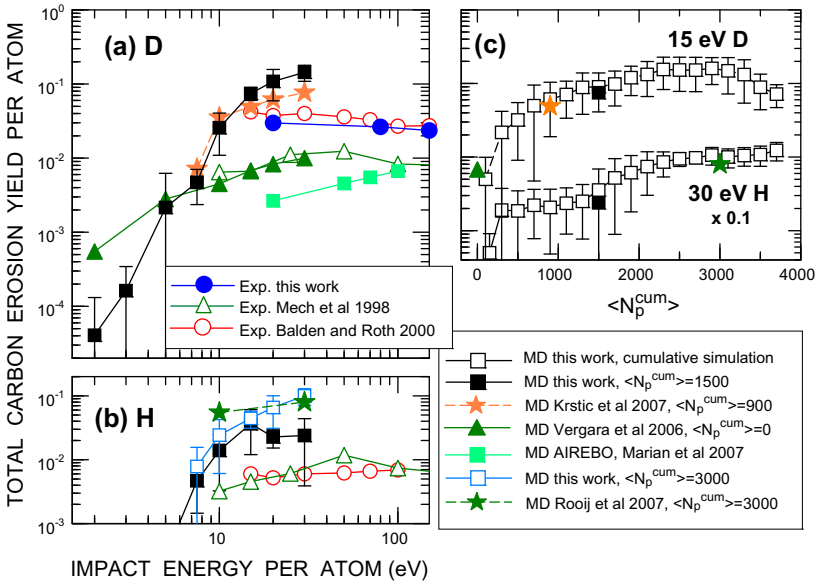

Fig. 6. (a) Total carbon erosion yield at room temperature for D impact of a-C:D (MD simulations) and D^+ impact of ATJ graphite (experiment) as a function of impact energy. (b) same as (a) but for H impact of a-C:H. (c) Total carbon erosion yield for 15 eV D impact and 30 eV H impact as a function of average fluence, $\langle N_p^{cum} \rangle$. The error bars represent the standard deviation of the results for six surfaces (for simplicity only present error bars are displayed). Our measurements and calculated yields for a mean fluence of $\langle N_p^{cum} \rangle = 1500$ and $\langle N_p^{cum} \rangle = 3000$ are compared with previously calculated yields for $\langle N_p^{cum} \rangle = 0$ [11], $\langle N_p^{cum} \rangle = 900$ [18], $\langle N_p^{cum} \rangle = 3000$ [22], and MD results using the AIREBO potential and $\langle N_p^{cum} \rangle = 0$ [23]. Because experimental data are scarce we also display previous measurements for D_2^+ and D_3^+ impact (Fig. 6a) and H_2^+ and H_3^+ impact (Fig. 6b) of Mech et al. [15] and Balden and Roth [14] on various carbon materials (points for the latter are not actual data but represent the average over a large amount of experimental data points). The yields and impact energies are scaled accordingly as yield/D vs. E_p/D.

better statistics are needed to compute smaller yields (e.g. for individual hydrocarbon emission). The statistical significance can be improved dramatically by using the surfaces prepared by cumulative bombardment and performing a large number of short time (~5 ps) independent non-cumulative single particle impact simulations on each surface (see our previous work [18,21] for additional details). Here we use six surfaces created with fluences of $N_p^{cum} = 1000, 1200, 1400, 1600, 1800,$ and 2000 (an average fluence of $\langle N_p^{cum} \rangle = 1500$) and perform N_p = 2000–4000 independent (non-cumulative) trajectory simulations on each surface which translates into N_p = 12,000–24,000 total trajectories (or a statistical improvement of a factor of $\sqrt{12}$–$\sqrt{24}$). We have verified that statistically significant yields obtained from the two different simulations are approximately consistent with each other (see, e.g., discussion of Fig. 6 below).

3. Experiment

The experimental apparatus used in this work has been described previously (see [28–30] for details). All measurements were performed in a floating potential ultra-high vacuum chamber with base pressures in the 10^{-8} Pa range, into which decelerated ion beams from an ECR ion source can be directed [31]. A sensitive quadrupole mass spectrometer (QMS) was installed in the scattering chamber to detect the emission of deuterium, methyl radicals, and CD_4, C_2D_2, C_2D_4, C_2D_6, C_3D_6, and C_3D_8 hydrocarbons. The beam was well defined spatially (FWHM ~4 mm below 60 eV/D) and in energy. As discussed elsewhere [32], the relative energy spread of the decelerated beams was less than 10% down to a final energy of 10 eV and typically below 20% at lower energies, as measured using an electrostatic spherical sector spectrometer. Fluxes in excess of 1×10^{15} D/(cm^2 s) were obtained for energies as low as 10 eV/D. The deuterium ion beams impacted the sample at normal incidence.

The QMS, which was interfaced to a Macintosh-based data acquisition system, was used to measure mass distributions in the 1–80 amu mass range at fixed intervals in time, or alternatively, to follow the intensity of selected mass peaks vs. beam exposure time. The evolution of peak intensities was measured vs. accumulated beam fluence until steady-state conditions were reached. The incident ion intensity was determined from a direct current reading on the target sample. The procedure used to deduce the partial chemical sputtering yields was described in detail in [28]. It involves selection of an analysis mass for identification of each species of interest, determining and correcting for the possible interferences due to cracking of heavier hydrocarbons, and placing the production yields on an absolute scale using calibrated leaks. The procedure is expressed by the equation $\underline{\mathbf{y}} = \mathbf{R}(\mathbf{C}^{-1}\underline{\mathbf{s}})$, where $\underline{\mathbf{y}}$ is the apparent production yield array for the selected hydrocarbons, $\mathbf{C}$ is the cracking pattern matrix, and $\mathbf{R}$ is the diagonal calibration matrix giving the conversion from QMS normalized peak height to production rate in particles/s. The vector $\underline{\mathbf{s}}$ is the array of measured peak heights (normalized to the incident ion flux, expressed in particles/s) at each analysis mass. To obtain true partial chemical sputtering yields, the apparent yields must be corrected for wall contributions originating from the small fraction of incident ions that is reflected from the sample and subsequently ejects hydrocarbon precursors from the walls of the vacuum chamber which can then contribute to the QMS signal (see [28] for details on subtracting these wall contributions). Since many of the peak intensities at the analysis masses for the heavier hydrocarbons were low, poor signal-to-noise ratios prevented reliable estimation of wall contributions for these species [33]. The heavier hydrocarbon production yields presented here are therefore quoted without corrections for wall contributions. Total C erosion yields deduced from the summed hydrocarbon yields as well as CD_3/CD_4 production yields have been reported in [13]. All quoted yields represent steady-state values reached after beam exposures to fluences in excess of 10^{18}/cm^2.

The ATJ graphite (UCAR Carbon Co.) target could be electron-beam heated from the rear. For these targets, sample annealing at temperatures in excess of 1200 °C was performed, as determined

using a calibrated infrared (IR) thermal monitor, in order to reinitialize the sample after each measurement condition.

4. Results and discussion

Figs. 6a and 6b depict calculated total carbon erosion yields at room temperature for D impact of a-C:D and H impact of a-C:H, respectively. The figure illustrates that the calculated yields are very sensitive to the fluence. The present results for D impact using $1000 < N_p^{cum} < 2000$ are slightly larger than our previous calculations [18] using $400 < N_p^{cum} < 1400$. More notably, these are very different from the yields calculated using $N_p^{cum} \sim 0$, i.e., unsaturated surfaces [11]. Note, however, that these calculations are consistent with each other as shown in Fig. 6c, which depicts the total carbon erosion yield as a function of average fluence. The present calculations at various fluences agree with previous calculations in the appropriate range of fluence. The present simulations for D impact using $\langle N_p^{cum} \rangle = 1500$ are closer to a supersaturated regime while those in [11] are far from this regime and much smaller in magnitude. Calculations using the REBO potential and $N_p^{cum} \sim 0$ predict a considerably larger yield than those of Marian et al. [23] for $N_p^{cum} \sim 0$ and using the AIREBO potential [34]. These AIREBO calculations seem to underestimate experimental data but its dependence on N_p^{cum} is unknown and better agreement might be found for supersaturated surfaces. Figs. 6b and 6c show that our results for H impact using supersaturated surfaces with $\langle N_p^{cum} \rangle \sim 3000$ are consistent with MD simulations in the supersaturated regime by Rooij et al. [22]. Fig. 6b shows that yields for H impact at $\langle N_p^{cum} \rangle = 1500$ do not increase with increasing energy above 15 eV. This happens because, at these energies, quasi-steady-state supersaturation by H impact is reached at fluences higher than $\langle N_p^{cum} \rangle = 1500$ (see Fig. 6c and structures in Fig. 2c). Yields obtained from our cumulative simulations in the range $\langle N_p^{cum} \rangle = 3000$ agree with our $\langle N_p^{cum} \rangle = 1500$ calculations only below 20 eV but increase with energy above 15 eV.

Fig. 6a also displays new measurements of the total carbon erosion yield for D^+ impact of ATJ carbon. These experimental data are similar in magnitude to previously measured total erosion yields (per D) for D_3^+ impact on various carbon surfaces by Balden and Roth [14] but about a factor of three larger than those measured for pyrolytic graphite by Mech et al. [15]. Note, however, that Balden and Roth [14] and Mech et al. [15] agree with each other for H impact (Fig. 6b). The figure shows that the measured yields are smaller than the present calculated yields for supersaturated surfaces for both D and H impact for $E_p > 10$ eV.

Fig. 7 sheds some light on the origin of the discrepancy by separating the total yield into its component yields for emission of hydrocarbons containing one (Fig. 7a), two (Fig. 7b), or three (Fig. 7c) C atoms. For example, the total carbon erosion yield for H impact, Y^H_{totC}, can be expressed as a sum

$$Y^{\mathrm{H}}_{totC} = \sum_{n\geqslant 1}\sum_{x\geqslant 0} n\, Y^{\mathrm{H}}_{\mathrm{C}_n\mathrm{H}_x} \tag{2}$$

of the yields $Y^{\mathrm{H}}_{\mathrm{C}_n\mathrm{H}_x}$ for emission of C_nH_x molecules. Fig. 7a–c display fractional yields for $n = 1,2,3$ and are labeled as $\sum_{x\geqslant 0} nY_{\mathrm{C}_n x}$ to indicate fractional yields for each impacting species, i.e., $\sum_{x\geqslant 0} n Y^{\mathrm{H}}_{\mathrm{C}_n\mathrm{H}_x}$, $\sum_{x\geqslant 0} n Y^{\mathrm{D}}_{\mathrm{C}_n\mathrm{D}_x}$, or $\sum_{x\geqslant 0} n Y^{\mathrm{T}}_{\mathrm{C}_n\mathrm{T}_x}$.

While the best agreement between simulation and measurement is found for fractional emission of hydrocarbon molecules containing a single C atom (Fig. 7a), the calculations appear to overestimate all the fractional yields. This overestimate increases for molecules containing two and three C atoms (Figs. 7b and 7c). The measured yields decrease very rapidly in magnitude with the number of C atoms. Similar trends were found by Mech et al. [35] and Macauley et al. [26] at low energies and room temperature targets and by Yamada [36] at higher energies and higher target temperatures. The three C atom yields for D_2^+ and D^+ appear to show significant differences at the lowest investigated energy. The measurement for D_2^+ at that energy was made with higher beam current per D than the D^+ measurement, leading to improved signal-to-noise conditions for the measurement for D_2^+. Although not shown in the figure, we obtained a similar yield per D at that energy with D_3^+, leading us to give greater credence to the D_2^+ result at 20 eV. In contrast, the calculated yields decrease very slowly with n and for $n < 5$ the different component yields contribute nearly equally to the total yield. As evident in Fig. 7, the higher the number of C atoms, the larger the fluctuations of the corresponding C yields due to the poorer statistics for ejecta with larger n.

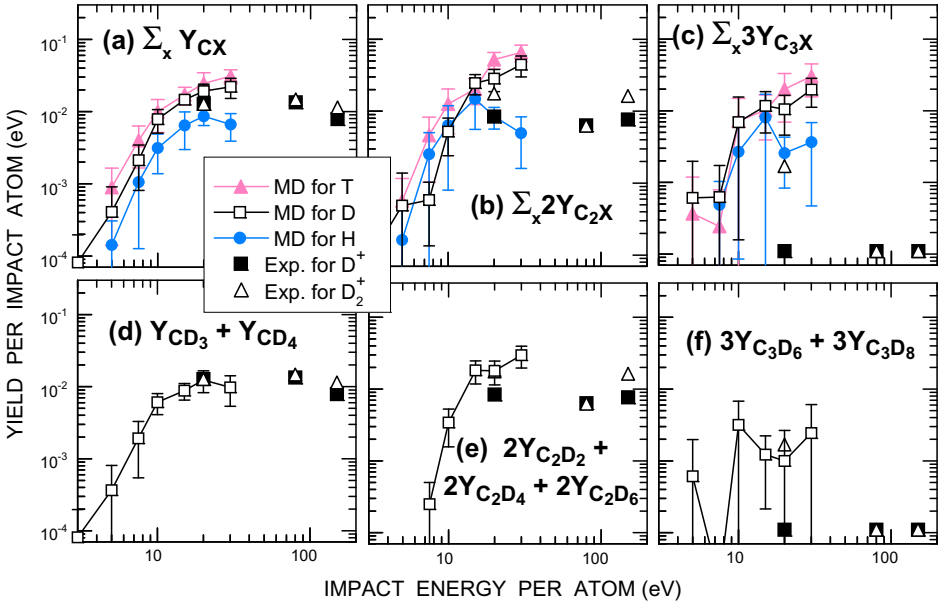

Fig. 7. Relative contribution to the total yield associated with molecules containing one (a), two (b), and three (c), carbon atoms for H, D, and T impact (MD simulations) and D^+ and D_2^+ impact of ATJ graphite (experiment) as a function of impact energy. (d–f) display the indicated subset of the sum of the yields (see text).

The overestimation of the calculated yields, particularly of the large hydrocarbons represents an open problem. The agreement with experiment improves when a direct comparison is made for only those molecules that are experimentally analyzed (see Figs. 7d–7f), which typically exclude low hydrogenation, unstable radicals. For example, of all the possible 3C containing molecules, the experiment only measures C_3D_6, and C_3D_8. Above 10 eV, the sum of the calculated yields for these two molecules agree with the summed measured yields within the uncertainties. However, the sum of the simulated yields for these two molecules accounts for only ~10% of the total simulated yield of molecules containing three C atoms. While it is possible that the less saturated (radical) molecules stick to the stainless steel walls or baffle in the experiment (see the concluding remarks for additional discussion) and thus are not detected, resulting in an underestimation by experiment, an overestimation by the simulation is more likely for C_3D_x molecules, since the calculated results exceed not only the yields deduced in the present measurements, but also total mass loss results of Balden and Roth based on a microbalance technique [14]. An important reason for this overestimation could be a poor parameterization of the potential for reactions leading to the complex hydrocarbons. Also, the current parameterization of the REBO potential does not correctly reproduce the shape of the screened Coulomb repulsion between atoms at close distances and atoms which probe this region of the potential are not properly deflected. Pathways for improving the simulations are discussed in the concluding remarks along with other outstanding issues. In addition, quasi-steady-state supersaturation by H impact is reached at fluences higher than $\langle N_p^{cum} \rangle = 1500$, which leads to a drop of the yields at the highest calculated energies displayed in Fig. 7. Due to these potential problems, in the following we focus on our calculated yields for the reduced range $E_p \leqslant 15$ eV. The shortcomings of the simulations are not expected to lead to isotopic differences in this energy range.

Fig. 8 compares our calculated isotope enhancements Y^D/Y^H and Y^T/Y^D with previously measured and predicted enhancements at room temperature. Because data on isotope enhancements are scarce we display previous results for various carbon-based materials and for atom and molecule impact (the impact energies are scaled accordingly). For clarity, calculated error bars are not displayed (note, however, that our calculations at 5 eV have very large statistical uncertainties). Previous results for the Y^D/Y^H enhancement (Fig. 8a) range from little enhancement [12] to close to an order of magnitude enhancement [14,3]. Our Y^D/Y^H calculated enhancement factor ranges from ~2 to 3 and is in good agreement with the predictions of Liang et al. [2] and Salonen et al. [9]. As expected, the Y^T/Y^D enhancement (Fig. 8b) is smaller than the Y^D/Y^H enhancement due to the smaller relative mass change. Our calculated Y^D/Y^H enhancement is in better agreement with the predictions of Liang et al. [2] and Salonen et al., [9], and are consistent with the higher energy measurements of [26]. The favorable comparison between our calculations and those in [9] suggests that the enhancement factor is insensitive to whether or not the surfaces are supersaturated or whether the saturating atoms at the surfaces are of the same species as the projectile.

Fig. 8 provides not only a good illustration of the current uncertainties on isotope enhancements but also of the low-energy limitations of simplified models of sputtering. As described by Hopf and Jacob [3], TRIM.SP calculations were incorporated into a model for the energy dependence of chemical sputtering that requires as input parameter the energy transfer required to break a C–C bond (typical C–C bond energies in hydrocarbon molecules are ~5 eV). However, such models based on energy/momentum transfers in sequential two-body interactions (i.e. Eq (1)) break down for impact energies approaching the threshold for breaking C–C bonds. As we show next, the physics/chemistry at the root of near-threshold bond-breaking is inherently a many-body problem (i.e. at least a third body is needed at the lowest impact energies). This is illustrated by analyzing the more manageable problem of C–C bond-breaking of simple hydrocarbons in atom-molecule collisions using our MD approach. While limited in applicability, this approach is useful for discussing some aspects of the multibody process arising from the empirical REBO potential and helps to understand the MD results. Admittedly, REBO is an average bond-order potential only expected to lead to statistically acceptable results in bulk interactions. Nevertheless, even though no quantitative accuracy is intended for these reductions to atom-(small) molecule collision processes, insight into qualitative behaviors can be gained.

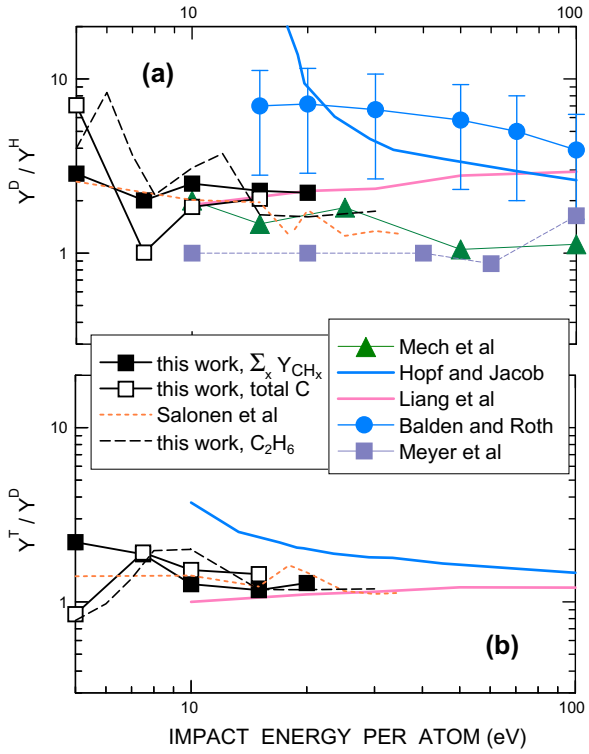

Fig. 8. Isotope enhancement of the sputtering yields at room temperature: (a) Ratio of the sputtering yield for D impact to that for H impact. (b) Ratio of the sputtering yield for T impact to that for D impact. Present results obtained for total C erosion yields and for sputtering of hydrocarbons with a single C atom (CH_x) are compared with MD calculations for total erosion of a-C:H of Salonen et al. [9], theoretical predictions by Liang et al. [2] and Hopf and Jacob [3], measured yields of methane of Meyer et al. [12] and total erosion of Mech et al. [12] for H_2^+ and D_2^+ and measured total erosion data of Balden and Roth [14] for H_3^+ and D_3^+ impact on various carbon materials (points and error bars are not actual data but represent the spread over a large amount of experimental data points). Also displayed in the figure are present results for the ratios of the bond-breaking cross sections by in collisions of H, D, and T impact of C_2D_6 (see text).

Fig. 9a displays calculations of C–C bond-breaking cross sections in collisions of H, D, and T with ethane (C_2H_6, C_2D_6, and C_2T_6, respectively). These calculations were performed using the same REBO potentials as were used in our MD simulations for a uniform beam of projectiles incident with a random impact parameter and colliding with a randomly oriented ethane molecule initially in its ground ro-vibrational state. One advantage of this simpler collision system is that a much larger number of trajectories can be computed in a short time to study weak reactions near threshold (up to a million trajectories have been used). At $t = 0$ the molecule was placed with its center of mass at the origin of coordinates ($x = 0$, $y = 0$, $z = 0$) and its orientation was chosen at random by rotating the molecule with three random Euler angles. The projectile was initially placed at a large distance z from the molecule

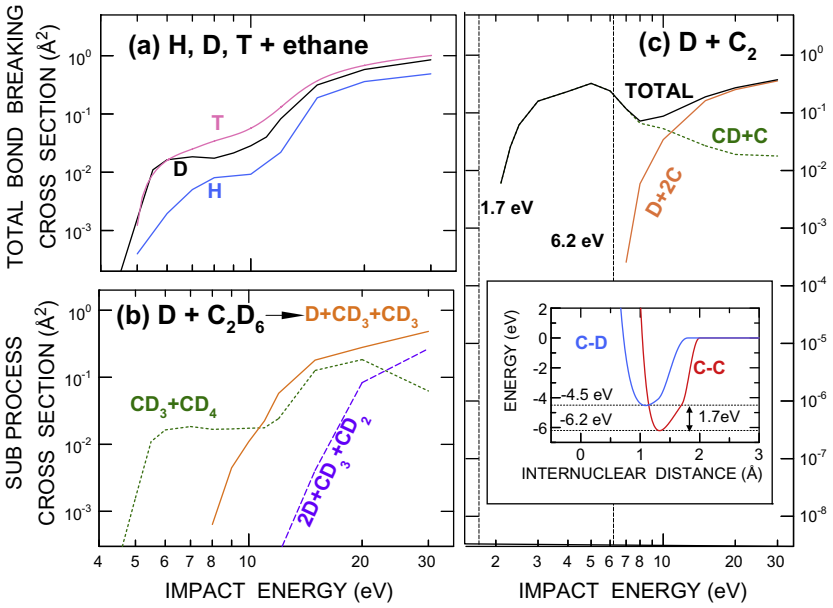

Fig. 9. (a) Total C–C bond-breaking cross sections in $H + C_2H_6$, $D + C_2D_6$, and $T + C_2T_6$ collisions as a function of impact energy. (b) Cross sections for the different reaction channels leading to C–C bond-breaking in $D + C_2D_6$ collisions. (c) C–C bond-breaking cross sections in $D + C_2$ collisions. The inset shows the C–C and C–D potential energy diagrams that determine the bond-breaking thresholds.

and a random impact parameter $\rho = \sqrt{x^2 + y^2}$ and polar angle $\varphi = \arctan(y/x)$. In order to represent a uniform beam, φ was chosen uniformly in $[0, 2\pi]$ and ρ^2 was chosen uniformly in $[0, \rho^2_{\max}]$, where $\rho_{\max}$ is an impact parameter above which no chemical reaction takes place. The cross section for C–C bond-breaking (BB) is simply given by $\sigma_{BB} = \pi\rho^2_{\max} N_{BB}/N_P$, where N_{BB} is the number of collisions that result in BB and N_p is the total number of projectile trajectories (the same expression applies to any other process).

Fig. 9a shows that isotope effects are clearly present in this simple collision system studied using the REBO potential (similar effects are found for all hydrocarbons). Moreover, the isotope enhancements of the cross section for ethane (also depicted in Fig. 8) are similar to the enhancements observed in full MD sputtering simulations. Fig. 9b shows that C–C bond-breaking can take place through different reaction channels, e.g.,

$$\begin{aligned} D + C_2D_6 &\rightarrow CD_3 + CD_4 \\ &\rightarrow D + CD_3 + CD_3 \\ &\rightarrow 2D + CD_2 + CD_3 \\ &\rightarrow \cdots \end{aligned} \tag{3}$$

where the final products are in any ro-vibrational state. Moreover, Fig. 9b shows that each reaction channel has a different threshold. The same observation applies to the even simpler collision system of $D + C_2$ which has only two reaction channels. (see Fig. 9c). The threshold energy for the D + 2C channel is close to the C–C REBO bond energy, $E_b[C_2] \sim 6.2$ eV. However, the dominant channel at low energies is the C + CD channel which involves a (associative) particle transfer process and has a threshold near $E_b[CD]$–$E_b[C_2] \sim$ 1.7 eV. Such an associative particle transfer process is beyond the scope of two-body dynamics and is always the dominant bond-breaking channel at low energies (see also Fig. 9b for ethane), although the exact threshold energies depend on the binding energies of the reactants. The presence of this associative–dissociative channel at low energies was also found in previous MD simulations [9,10].

A similar picture holds for chemical sputtering. As long as associative–dissociative exit channels such as $D + R\text{–}CD_x \rightarrow R\text{–}D + CD_x$ or $R + CD_{x+1}$ are open, these provide the lowest energy bond-breaking thresholds because they require less energy than the three-body break-up channel $D + R\text{–}CD_x \rightarrow R + D + CD_x$. It is noteworthy that the thresholds for all these reactions are nearly mass independent since they are given just by the difference between the initial and final binding energies of the molecules in the entrance and exit channels. Small deviations from this mass independence occur because the available kinetic energy in the entrance channel is slightly smaller than the incident projectile energy due to energy and momentum conservation of the center of mass of the entire collision system. Deviations can also occur because the quantum vibrational modes of the molecules in the exit channel are mass dependent. In contrast, models based on sequential binary collisions predict a mass dependent threshold since the maximum energy transferred in a binary collision to break a bond (Eq. (1)) is mass dependent. This is the origin of the large isotope effect predicted by Hopf and Jacob [3]. However, near the associative–dissociative threshold, C–C bonds are broken as the projectile enters the region around two bonded carbon atoms and transiently weakens the binding interaction between the carbon atoms [9]. The mass dependence arises because the heavier projectiles are slower moving (at constant incident energy) and thus have a longer time to remain as a perturbative effect on the C–C bond and to find the exit reaction pathway leading to attachment to one of the C atoms. Very close to threshold, however, all projectiles with appropriate collision geometry remain in the interaction region a sufficiently long time and the only factor affecting the cross section is the fraction of collision geometries that access the reaction channel.

Fig. 9 shows that the thresholds for C–C bond-breaking of C_2D_6 and C_2 are very different. The low-energy behavior of the total erosion yield (Fig. 6) is closer to that of the bond-breaking cross section for C_2D_6 because C bonds near the surface are saturated and have C–C bonding energies of ~4–5 eV, which are closer to that of C_2D_6. This observation is also consistent with the change in the rate of decrease of the yield for different levels of saturation of the surface (i.e. $\langle N_p^{cum} \rangle = 1500$ compared with $\langle N_p^{cum} \rangle = 0$ in Fig. 6a). Clearly, chemical sputtering does not possess a precise threshold with well defined structures but rather has a series of thresholds for breaking C–C bonds of all $R\text{–}CD_x$ moieties. The precise behavior at low energies depends on the number density and

binding energies of such moieties, as well as the surface temperature which determines the initial vibrational energies. It is noteworthy, however, that the distribution of moieties prepared by the different projectiles was found to be nearly independent of projectile mass. Thus, the mass dependence of the erosion yields at low energies appears to be dominated by the mass dependence of the elementary bond-breaking chemical reactions.

In addition to emission of carbon compounds, hydrogen impact of supersaturated carbon leads to emission of hydrogen atoms and molecules (Fig. 10). The yields for emission of H, D, and T due to H, D, and T impact, respectively, correspond to the respective reflection coefficients and together with H_2, D_2, and T_2 emission provide the dominant hydrogen emission processes below the C–C bond-breaking thresholds. Fig. 10 shows that the yields exhibit a clear isotope dependence above ~3 eV which vanishes at the lowest impact energies. The origin of this behavior is very similar to that discussed for breaking C–C bonds. Because the simulations are performed near the steady-state regime of supersaturation where little additional hydrogen can be retained by the surface, below ~7 eV $Y^{H}_{H} \approx 1 - 2Y^{H}_{H_2}$ and a similar relationship applies for D and T impact. (At higher energies, inclusion of chemical sputtering again gives total steady-state hydrogen containing yields close to unity, $Y^{H}_{totH} = \sum_{n\geqslant 1}\sum_{x\geqslant 1} x Y^{H}_{C_nH_x} + 2Y^{H}_{H_2} + Y^{H}_{H} \approx 1$). Thus, the behavior of the reflection coefficients and of H_2, D_2, and T_2 emission are connected via particle conservation. Close to their respective thresholds, the hydrogen molecules are emitted via associative–dissociative processes where C–H, C–D or C–T bonds are broken, e.g. R–H + H → R + H_2, and does not involve multiple reaction channels. Fig. 10 shows a mass independence near threshold that is more evident than for sputtering of C−C ontaining species. This happens because both the threshold energy and the slope near threshold are mass independent (the latter is not as steep as for C–C bond-breaking). Compared to hydrocarbon emission, H_2, D_2, and T_2 emission events are much more numerous and thus have much smaller statistical uncertainties.

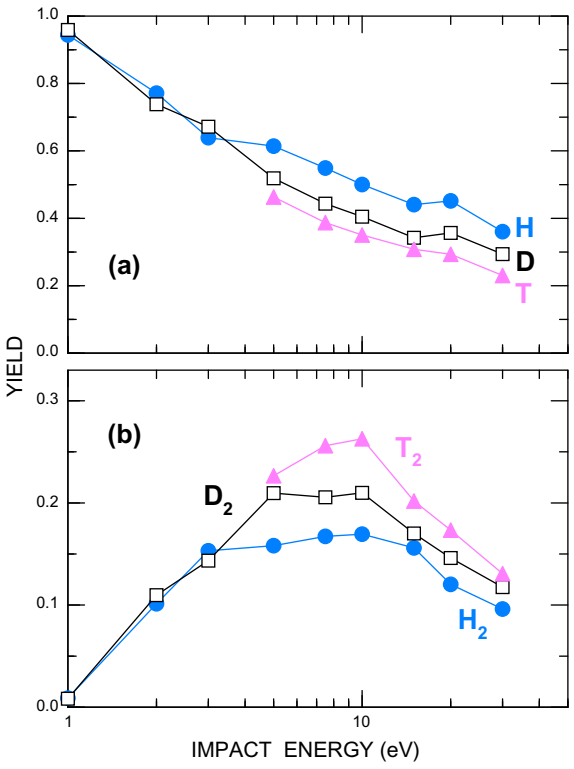

Fig. 10. Total yields for emission of H, D, and T (a) and H_2, D_2, and T_2 (b) due to impact of H, D, and T, respectively. The data in (a) is equivalent to the reflection coefficient.

Because most of the experimental studies of isotope effects have been performed with molecular projectiles, we have also performed cumulative and sputtering MD simulations for H_2^* and D_2^* projectiles. These excited projectiles were prepared in a dissociated state with an initial internuclear separation of 2 Å (close to the REBO cutoff radius) to approximate the vibrationally excited neutral molecules expected to be formed by electron capture from the surface [20]. We found that for such excited molecules the surface characteristics during cumulative molecular impact simulations and the carbon erosion yields per atom are very similar (within statistical uncertainties) to those for atom impact, in agreement with previous work [20]. That is, $2n$ H impacts at an energy E_H appear to be approximately equivalent (within statistical errors) to n H_2^* impacts at an energy $2E_H$. This is in contrast to recent low-energy measurements by Vergara et al. [11], which showed a significant molecular size effect of up to a factor of two in comparing methane yields for same energy/D of D^+ and D_3^+ projectiles at 10 eV/D. The reason for these differences with the present simulations is currently not understood and will be explored in further theoretical and experimental research. It appears that any enhancement due to molecular impact is sensitive to the chemical structure of the interface since MD simulation results for unsaturated surfaces by Nordlund's group [11] showed an almost order of magnitude enhancement at 30 eV/D of D_3-induced total C yields over those produced by D impact.

5. Conclusions and outlook

The present classical MD simulations using the many-body REBO potential have shown that chemical sputtering yields of supersaturated carbon increases with projectile mass, but not as dramatically as that predicted by simpler models based on sequential binary collisions. Only a weak dependence on the mass was found in the number of moieties of supersaturated surfaces created by cumulative bombardment and, thus, the root of the mass dependence was found to be directly related to the probability for breaking the C–C bonds that attach such moieties. Much of the behavior at low energies in full MD simulations was found to be qualitatively similar to that for bond-breaking reactions in collisions of hydrogen isotopes with simple saturated hydrocarbons. One important conclusion is that the threshold energies for breaking C–C bonds are nearly mass independent within the many-body REBO potential model.

Our measured yields are consistent with previous measurements of Balden and Roth [14] and provide new insights into the relative contributions to the total yield as a function of the number of carbon atoms in the ejected hydrocarbons. Consistent with previous findings [18], the present MD simulations for supersaturated carbon surfaces agree with experiment for the total yield of hydrocarbons containing a single carbon atom. However simulations greatly overestimate the yield of molecules containing three carbon atoms at impact energies above 20 eV. The origin of this disagreement is an open problem. We have shown that our simulations are relatively stable with respect to the parameters of our cumulative bombardment scheme. However, it is evident that MD simulations are quite sensitive to the form and parameters of the many-body potentials (see Fig. 6). The REBO potential used in this work provides a good empirical description of covalent bonds for nonpolar systems, treats contributions to the bond order in radical species, and was fit to vibrational frequencies of some molecular hydrocarbons and the elastic constants of bulk carbon-based materials [27]. However the present parameterization incorrectly reproduces the shape of Coulomb repulsion between atoms

at close distances, which becomes an important factor for energies greater than 15 eV for H–H interactions. In addition, the REBO potential neglects non-bonded interactions, including torsional and van der Waals forces incorporated in the more advanced AIREBO potential [34]. Very few particle–surface calculations using AIREBO are available in the literature because they are considerably more computationally involved that those using REBO. For unsaturated surfaces the yields obtained using AIREBO by Marian et al. [23] at ~20 eV are a factor of ~3 smaller than those using unsaturated surfaces and REBO potentials (see Fig. 6). It is not known whether AIREBO simulations would have improved agreement with measurements of the total erosion yields above 10 eV if supersaturated surfaces were employed. The systematic inclusion of more C_nH_y hydrocarbon parameters, bonding energies, bonding lengths, barriers and vibration frequencies might also significantly improve both REBO and AIREBO potentials and yield better results in the sputtering of the complex hydrocarbons. Work exploring such extensions is currently underway.

The differences between REBO and AIREBO simulations are predominantly due to the larger repulsive barriers in the Lennard-Jones corrections incorporated in the AIREBO potential. These barriers make the interface more "impenetrable" and lead to reflection coefficients that are considerably larger than their REBO counterparts [37]. The inset in Fig. 11 provides an example of such a repulsive barrier by displaying the total potential energy of the D + C_2 system as a function of the distance between D and the center of mass of C_2. Fig. 11 shows that the C–C bond-breaking cross sections in D + C_2 and D + C_2D_6 collisions change considerably with the potential used, suggesting that the AIREBO Lennard-Jones barriers can dramatically affect the low-energy behavior of the sputtering yields. Saturation of the carbon bonds enhances the importance of these barriers, but it is not clear whether supersaturation would lead to larger or smaller erosion yields. For C_2D_6 (Fig. 10a) the D atoms in the target completely shield the C atoms and effectively block the associative–dissociative channel, thereby changing dramatically the bond-breaking threshold. At present, it is not clear whether REBO or AIREBO provides a better description of the bond-breaking process near threshold.

Another open problem concerns the relative importance of the sputtering yields of CD_3 and CD_4, which was also a case in our previous simulations [18,21]. While theory and experiment agree on the sum of the yields (i.e. Fig. 7), Fig. 12 shows that they disagree considerably in the ratio of these yields, Y_{CD_4}/Y_{CD_3}. The experimental spectrum [13] is dominated by CD_4 whereas the calculated spectrum is dominated by CD_3. This discrepancy is presently not understood. Experimentally, the ejected particles coming from the target surface are reflected at least once from the stainless steel walls or baffle in the experimental geometry prior to detection. These walls are likely coated with deuterium and deuterated hydrocarbons and CD_3 could be passivated by wall collisions by capturing an additional D atom during reflection. The present QMS data preferentially reflect the partial pressures of low sticking species that have undergone (and possibly have been modified by) wall collisions, and less so species with a high sticking probability (see [1] for a detailed discussion). For hydrocarbon film surfaces at least, the methyl sticking coefficient was found to be quite low ($\sim 10^{-4}$) [38]. Nevertheless, work is underway to use a direct line-of-sight time-of-flight spectrometer to analyze this problem. This may also shed some light about the actual emission spectra of two and three carbon atom containing molecules, for which theory predicts a dominance of radical species.

Theoretically, we have shown earlier [18] a correlation between the energy dependence of the yield of sputtered CD_3 and the number of terminal R–CD_3 moieties. For impact energies near the threshold for ejecting hydrocarbons, CD_4 originates only from D + R–CD_3 → R + CD_4 reactions. In turn, CD_3 can originate from not only the same entrance channel as D + R–CD_3 → R–D + CD_3 or D + R–CD_3 → R + D + CD_3 but also from R–CD_2 moieties as D + R–CD_2 → R + CD_3. This greater number of exit channels leading to CD_3 in sputtering simulations results in a ratio $Y_{CD_4}/Y_{CD_3} < 1$ at all impact energies. For increasing impact energies where a collision cascade takes place, complete break-up processes dominate over associative–dissociative processes and increases even further the abundance of CD_3 relative to that of CD_4. Also shown in Fig. 12 is the ratio of the C–C bond-breaking cross sections for producing CD_3 and CD_4 in D + C_2D_6 collisions. The trend of this ratio is similar

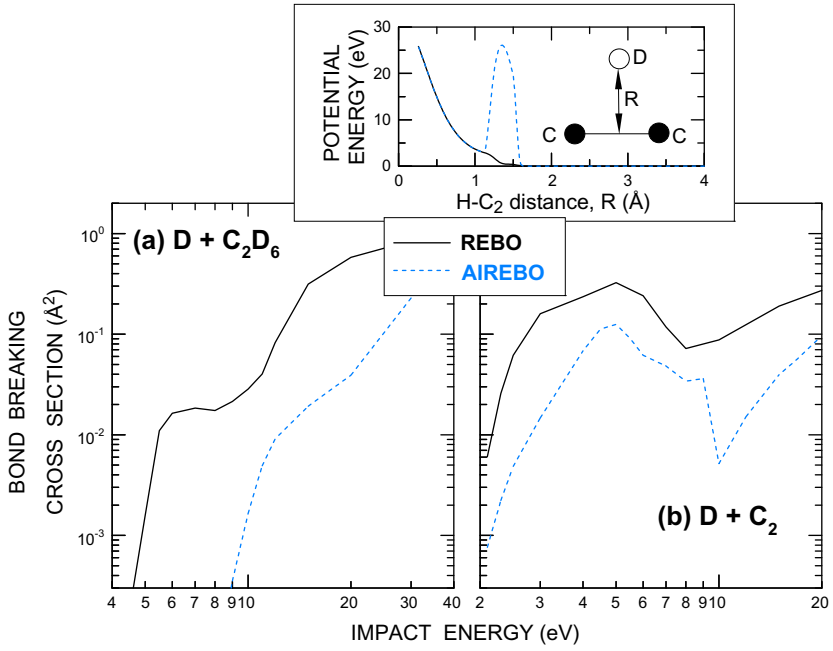

Fig. 11. Calculated total C–C bond-breaking cross sections in D + C_2D_6 (a) and D + C_2 (b) collisions using the REBO and AIREBO potentials. The inset shows the potential energy of a D atom interacting with a C_2 molecule with a fixed bond distance of 1.3 Å as a function of the distance between the D atom and the center of mass of the C_2 molecule for the two potentials. Note the prominent potential barrier for the AIREBO potential.

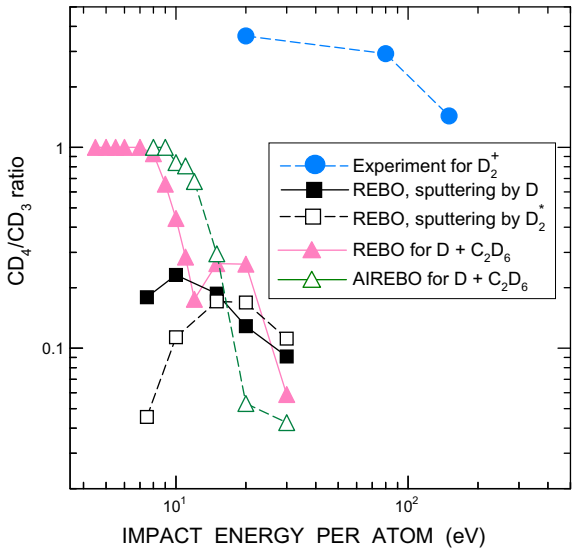

Fig. 12. Ratio between yields for emission of CD_4 and CD_3 resulting from the impact of D, D_2, and D_2^+ on supersaturated carbon surfaces at room temperature as a function of impact energy per atom. Also shown is the ratio of the cross sections for production of CD_4 and CD_3 in collisions of D with C_2D_6.

to that observed for the ratio of sputtering yields at high energies but tends to unity at low energies because the dominant associative–dissociative channel leads to an equal amount of CD_3 and CD_4. In actual sputtering simulations other channels can produce CD_3 (e.g. D + R–CD_2 → R + CD_3), resulting in a low-energy ratio that is smaller than unity. It is noteworthy that the ratio of the cross sections is fairly independent of the potential (REBO or AIREBO). The only additional mechanism that could increase the abundance of CD_4 for sputtering would be collisional hydrogen capture by detached CD_3 molecules on their way to escaping into vacuum. In our MD simulations with the present potentials, however, we have not found significant evidence for the dominance of this process.

Acknowledgements

We acknowledge support by the OBES and OFES of the US DoE under contract No. DE-AC05-00OR22725 with UT-Battelle, LLC, and partial support through SciDAC. SJS acknowledges support by the NSF (CHE0239448) and the DOD (47539-CH-MUR). This work was partially performed through DoE INCITE and SciDAC.

References

[1] W. Jacob, J. Roth, Topics Appl. Phys. 110 (2007) 329.
[2] J.H. Liang, M. Mayer, J. Roth, M. Balden, W. Eckstein, J. Nucl. Mater. 363–365 (2007) 184.
[3] C. Hopf, W. Jacob, J. Nucl. Mater. 342 (2005) 141.
[4] A.A. Haasz, J.W. Davis, Fusion Sci. Technol. 50 (58) (2006).
[5] R.R. Rye, Surf. Sci. 69 (1977) 653.
[6] A.B. King, H. Wise, J. Phys. Chem. 67 (1963) 1163.
[7] B.J. Wood, H. Wise, J. Phys. Chem. 73 (1969) 1348.
[8] J.P. Biersack, W. Eckstein, Appl. Phys. A 34 (1984) 73.
[9] E. Salonen, K. Nordlund, J. Keinonen, C.H. Wu, Phys. Rev. B 63 (2001) 195415.
[10] E. Salonen, Molecular dynamics studies of the chemical sputtering of carbon-based materials by hydrogen bombardment, Ph.D thesis, University of Helsinki Report Series in Physics, HU-P-D97, 2002. <http://ethesis.helsinki.fi/>.
[11] L.I. Vergara, F.W. Meyer, H.F. Krause, P. Traskelin, K. Nordlund, E. Salonen, J. Nucl. Mater. 357 (2006) 9.
[12] F.W. Meyer, H. Zhang, M.J. Lance, H.F. Krause, Vacuum 82 (2008) 880.
[13] H. Zhang, F.W. Meyer, J. Nucl. Mater. 390–391 (127) (2009).
[14] M. Balden, J. Roth, J. Nucl. Mater. 280 (39) (2000).
[15] B.V. Mech, A.A. Haasz, J.W. Davis, J. Nucl. Mater. 255 (1998) 153.
[16] J. Roth, B.M.U. Scherzer, R.S. Blewer, D.K. Brice, S.T. Picraux, W.R. Wampler, J. Nucl. Mater. 93 (601) (1980).
[17] P. Träskelin, K. Nordlund, J. Keinonen, J. Nucl. Mater. 357 (2006) 1.
[18] P.S. Krstic, C.O. Reinhold, S.J. Stuart, New J. Phys. 9 (2007) 209.
[19] S.J. Stuart, P.S. Krstic, T.A. Embry, C.O. Reinhold, Nucl. Instrum. Methods B 255 (2007) 205.
[20] P.S. Krstic, C.O. Reinhold, S.J. Stuart, Europhys. Lett. 77 (2007) 33002.
[21] P.S. Krstic, C.O. Reinhold, S.J. Stuart, J. Appl. Phys. 104 (2008) 103308.
[22] E.D. de Rooij, U. von Toussaint, A.W. Kleynac, W.J. Goedheera, Phys. Chem. Chem. Phys. 11 (2009) 9823.
[23] J. Marian, L.A. Zepeda-Ruiz, N. Couto, E.M. Bringa, G.H. Gilmer, P.C. Stangeby, T.D. Rognlien, J. Appl. Phys. 101 (2007) 044506.
[24] A. Ito, H. Nakamura, Thin Solid Films 516 (2008) 6553.
[25] A. Ito, Y. Wang, S. Irle, K. Morokuma, H. Nakamura, J. Nucl. Mater. 390-391 (2009) 183.
[26] R.G. Macauley-Newcombe, A.A. Haasz, J.W. Davis, J. Nucl. Mater. 337–339 (857) (2005).
[27] D.W. Brenner, O.A. Shenderova, J.A. Harrison, S.J. Stuart, B. Ni, S.B. Sinnott, J. Phys.: Condes. Matter 14 (2002) 783.
[28] L.I. Vergara, F.W. Meyer, H.F. Krause, J. Nucl. Mater. 347 (2005) 118.
[29] F.W. Meyer, L.I. Vergara, H.F. Krause, J. Nucl. Mater. 337 (2005) 922.
[30] F.W. Meyer, H. Zhang, L.I. Vergara, H.F. Krause, Nucl. Instrum. Methods Phys. Res. B 258 (2007) 264.
[31] V.A. Morozov, F.W. Meyer, Rev. Sci. Instrum. 70 (1999) 4515.
[32] F.W. Meyer, L.I. Vergara, H.F. Krause, Phys. Scripta T124 (2006) 44.
[33] B.V. Mech, Ph.D thesis, University of Toronto, 1997, unpublished.
[34] S.J. Stuart, A.B. Tutein, J.A. Harrison, J. Chem. Phys. 112 (2000) 6472.
[35] B.V. Mech, A.A. Haasz, J.W. Davis, J. Nucl. Mater. 241–243 (1147) (1997).
[36] R. Yamada, J. Nucl. Mater. 145–147 (359) (1987).
[37] C.O. Reinhold, P.S. Krstic, S.J. Stuart, Nucl. Instrum. Methods B 267 (691) (2009).
[38] Matthias Meier, Achim von Keudel, J. Chem. Phys. 116 (5125) (2002).